The Effect of Bogie Positions on the Aerodynamic Behavior of a High-Speed Train: An IDDES Study

Jiabin Wang[1,2] · Guglielmo Minelli[3] · Xiujuan Miao[4] · Jie Zhang[1,2] · Tiantian Wang[1,2] · Guangjun Gao[1,2] · Sinisa Krajnović[3]

Abstract

In this study, an improved delayed detached-eddy simulation method has been used to investigate the aerodynamic behavior of the CRH2 high-speed trains (HST) with different first and last bogie positions. The results of the numerical simulations have been validated against experimental data obtained from a previous wind tunnel test, a full-scale field test and a reduced-scale moving model test. The results of the flow prediction are used to explore the effects of the bogie positions on the slipstream, wake flow, underbody flow and aerodynamic drag. Compared with the original HST model, the downstream movement of the first bogie, has a great effect on decreasing the slipstream velocity and pressure fluctuation aside the HST, especially around the lower part of the HST. Furthermore, the size of the longitudinal vortex structure and slipstream velocity in the near wake region also decrease significantly by moving the last bogie upstream. Additionally, the movement of the first and last bogies toward the HST center, effectively decreases the drag values of the head and tail car, while a lower effect is observed on the intermediate cars.

✉ Guangjun Gao
gjgao@csu.edu.cn

[1] Key Laboratory of Traffic Safety on Track of Ministry of Education, School of Traffic and Transportation Engineering, Central South University, Changsha 410075, China

[2] National and Local Joint Engineering Research Center of Safety Technology for Rail Vehicle, Changsha 410075, China

[3] Department of Mechanics and Maritime Sciences, Chalmers University of Technology, 41296 Gothenburg, Sweden

[4] College of Automotive and Mechanical Engineering, Changsha University of Science and Technology, Changsha 410076, China

1 Introduction

Slipstream, characterizing a highly turbulent non-stationary airflow (Sterling et al. 2008), quantifies the air movement induced by a high-speed train (HST) pass by. This turbulent slipstream causes velocity and pressure fluctuations, which in turn generates forces acting on nearby passengers, railway workers, track infrastructures, but also deteriorates the running stability when two HSTs pass each other (Baker et al. 2014a, b). According to the data published by Popc (2006), more than twenty accidents have occurred in the UK rail network from 1972 to 2005 because of the effect of train slipstreams on the trackside workers and passengers waiting on the platform, resulting in life losses and material damages. However, these effects of slipstream become more serious with the increasing operational speed of HSTs (Yang et al. 2015; Baker et al. 2001). In most countries with an advanced high-speed railway transportation system, such as Japan, Germany and France, the operational speed of HSTs have reached 300 km/h. Even in China, the Chinese standard EMU has ran up to 350 km/h between Beijing and Shanghai. Thus, the effects of slipstream requires full attention during the design stage of the HST.

In the past decades, a large number of studies have been conducted on the HST aerodynamic behavior using four kinds of techniques, e.g. full-scale field tests (Baker et al. 2014a, 2014b), reduced-scale moving model tests (Baker et al. 2001; Gilbert et al. 2013; Bell et al. 2015), wind tunnel tests (Weise et al. 2006; Bell et al. 2014, 2016a, b) and numerical simulations using computational fluid dynamics (CFD) (Hemida et al. 2005, 2014; Chen et al. 2019; Flynn et al. 2014). Due to the high cost of human and material resources required, the full-scale field tests are only used when other methods cannot provide reliable results. Furthermore, full-scale tests are not suitable in the development phase of new HSTs. Although the reduced-scale moving model tests can lower the experimental costs and allow for a better control of the experimental environment, compared to that in the full-scale field test, the measurements are also sensitive to the experimental equipment and the installation accuracy. Another alternative technique is wind tunnel test, in which particle image velocimetry (PIV), smoke or oil-film visualizations and TFI Cobra probes can be used to obtain detailed information about the slipstream and the wake flow of a HST (Bell et al. 2014). However, the relative motion between the HST and the ground is impossible to simulate in a conventional wind tunnel without a moving-belt (Fago et al. 1991). This significantly affects the underbody flow (Xia et al. 2017a; Zhang et al. 2016; Wang et al. 2018a) as well as the distribution of slipstream velocities (Bell et al. 2016a, 2016b). With the rapid development of the computer technology, CFD has been widely utilized to investigate the flow characteristics near a HST, such as the underbody flow (Wang et al. 2018a, b), the slipstream (Guo et al. 2018; Wang et al. 2019b) and the wake flow (Xia et al. 2017b; Chen et al. 2019). In fact, nowadays CFD is able to produce reliable results giving the possibility to investigate a multitude of variables and flow structures around the model considered.

Previous studies have shown that the HST's aerodynamic performance is mainly decided by the geometry, such as the slenderness ratio, the height of the nose tip, the width of the windshields and the change rate in the cross-sectional area of the head and tail car (Guo et al. 2018; Wang et al. 2018b; Xie et al. 2018; Bell et al. 2017). Moreover, the key designing parameters of the underbody structures, such as the cowcatcher shape (Niu et al. 2017), the inclined angle of the equipment cabin cover (Zhang et al. 2018a), the bogie complexity (Dong et al. 2019), the bogie cavity length (Wang et al. 2020), and the bogie fairing configuration (Wang et al. 2019a, b) have been found to play a dominant role on the turbulent flow structures beneath the HST, which thus significantly affects the train slipstream, wake

flow and aerodynamic forces. In countries with advanced high-speed railway systems, different types of HSTs with different positions of the first and last bogie are employed for the tasks of passenger transportation, as shown in Fig. 1. The installation positions of the first and last bogies greatly alters the underbody flow characteristics, thereby influencing the aerodynamic performance of the HST. Thus, this paper aims to compare the aerodynamic drag, slipstream and wake flow between HSTs with different positions of the first and last bogie, and to verify whether, and possibly how, the bogie position affects the aerodynamic performance of the HSTs considered. The key findings in the present study can also provide guidance for the vehicle engineers when developing a new HST. The concrete motivations of this study are summarized as below:

- The slipstream velocity and pressure distribution of the side flow of three HST configurations with different positions of the first and last bogies are studied, to explore how the downstream movement of the first bogie affects the safety level of the trackside workers and the passengers standing on the platform.
- The longitudinal vortex structures behind the HSTs are investigated for the three considered cases, to analyze how the upstream movement of the last bogie influences the wake flow.
- The aerodynamic drag values of HSTs with different bogie positions are compared, to identify whether the displacement of the first and last bogies in the streamwise direction contributes to a decreased propulsion energy.

The rest of the paper is organized as follows: in Sect. 2, the geometry, computational domain, boundary conditions, meshes, the results of the grid independence study, numerical method and algorithm validation are given. In Sect. 3, the slipstream velocity and pressure, wake structures and aerodynamic drag are analyzed for HSTs with different bogie positions. Finally, conclusions are drawn in Sect. 4.

2 Methodology

2.1 Geometry Models

To meet the standards for a valid slipstream measurement, the overall length of a HST should be at least 120 m and include at least a head car, two intermediate cars and a tail car (CEN European Standard 2013). Thus, a five-car grouped CRH2 HST model was adopted in the present study, as shown in Fig. 2a. In order to validate the accuracy of the

Fig. 1 HSTs with various positions of the first and last bogies in the countries having advanced high-speed railway system: **a** CRH3 in China, **b** AGV in Italy, and **c** N700 in Japan (Wikimedia 2006)
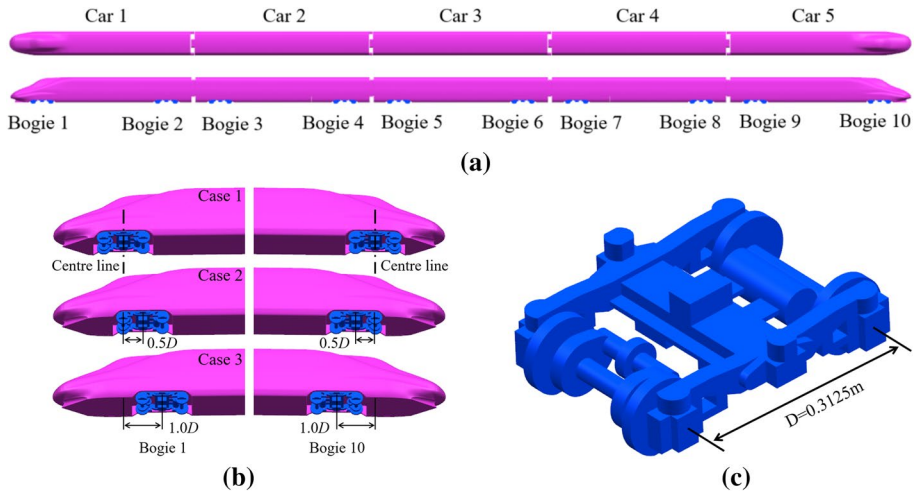
Fig. 2 HST models used in the numerical simulations: **a** original HST model, **b** comparison of different positions of the first and last bogies in three cases, and **c** bogie model

resolution of the mesh and methodology, the numerical results are compared with experimental results published by Zhang et al. (2018b). Thus, the same scale ratio of HST model of 0.125 was used in both wind tunnel tests and current numerical simulations. The height, defined as the characteristic length in the present numerical simulation, is $H = 0.4625$ m. The total length (L) and width (W) normalized by H are $L = 34.42H$ and $W = 0.91H$, respectively. To investigate the influence of the positions of the first and last bogie on the aerodynamic performance of the HSTs, two kinds of bogie positions were selected based on the original HST geometry (Case 1), as illustrated in Fig. 2b. This was done by moving downstream the first bogie and upstream the last bogie with a distance of 50% (Case 2) and 100% (Case 3) of the distance between two wheel axes $D = 68H$ (see Fig. 2c).

2.2 Computational Domain and Boundary Conditions

Figure 3 presents the computational domain and the related boundary conditions used for all numerical simulations. A uniform incoming flow with speed $U_{inf} = 60$ m/s is applied at the inlet, keeping the same Reynolds number used in the wind tunnel test (Zhang et al. 2018b). The Reynolds number was calculated based on the HST width H and incoming flow speed U_{inf}, being $Re = 1.85 \times 10^6$. A zero static pressure is given at the outlet. The lateral and upper walls are set as symmetry. The HST model is placed on a single-track ballast and rail (STBR) scenario (CEN European Standard 2013). The surfaces of HST model were treated as no-slip stationary walls, and the STBR and lower wall were set as no-slip moving walls with the same speed as the incoming flow. The dimensions of the domain and the positions of the HST model are described in Table 1 and Fig. 3.

2.3 Meshing Strategy

A hexahedral dominated mesh is designed for the numerical simulations. This type of mesh has been widely used for the numerical predictions of the aerodynamic forces (Niu et al. 2017;
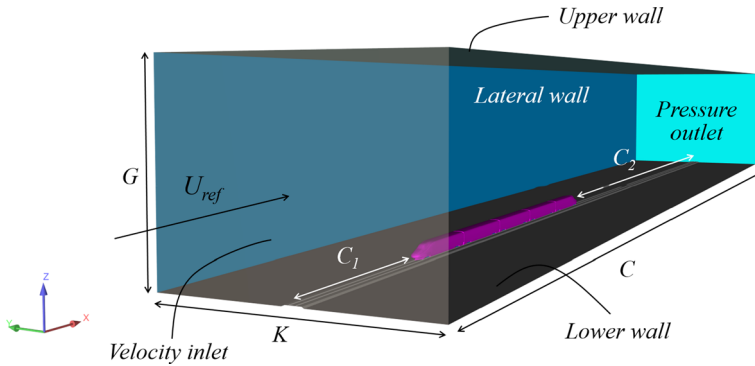
Fig. 3 Computational domain

Table 1 Dimension of the computational domain

C	C_1	C_2	K	G
104 H	20 H	50 H	24 H	16 H

Wang et al. 2019a, 2020; Zhang et al. 2018a), slipstream (Dong et al. 2019, 2020; Wang et al. 2019b) and wake flows of HSTs (Chen et al. 2019; Li et al. 2019; Xia et al. 2017a). Fifteen prism layers are used to accurately predict the turbulent boundary layer development along the HST, and the stretching ratio of the prism layers is set as 1.25, ensuring a good transition between the prism layers and the hexahedral mesh region, as described in Fig. 4b. Furthermore, two refinement boxes are used around the HST and in the wake region, as illustrated by the blue and magenta boxes in Fig. 4c, d. Specifically, the first refinement box (the magenta box) is adopted for refining the mesh resolution in the underbody region and wake region. The second refinement box is applied to refine the computational meshes around the HST. A coarse, a medium and a fine meshes are used to investigate the mesh independence of the numerical predictions. The mesh was not refined in the wall-normal direction (n^+) but only along the spanwise direction (Δl^+) and streamwise direction (Δs^+). Here, $n^+ = u_\tau n/v$, $\Delta s^+ = u_\tau \Delta s/v$ and $\Delta l^+ = u_\tau \Delta l/v$, where u_τ is the friction velocity, n is the distance between the first node and the HST surface in the wall-normal direction, Δl and Δs are the HST surface cell sizes in the streamwise and spanwise directions, and v is the kinetic viscosity. Table 2 describes the main features of each utilized mesh. The n^+_{mean}, Δs^+_{mean} and Δl^+_{mean} are the mean values of the n^+, Δl^+ and Δs^+ all over the surface of the model. In particular, n^+_{mean} was lower than 1.0. Only few elements at the streamlined part of the head car and sharp edges of the cowcatchers give n^+ values larger than 1.0 but lower than 2.3.

Table 3 shows the comparison of the drag force values of car 1 obtained by the current IDDES simulations with different grids on Case 1 (original model), previous wind tunnel tests (Zhang et al. 2018b) at Re $= 1.85 \times 10^6$. Note that the ground and STBR were set as stationary wall to reproduce the ground condition in the wind tunnel tests. The non-dimensional coefficient of aerodynamic drag is defined by Eq. (1).
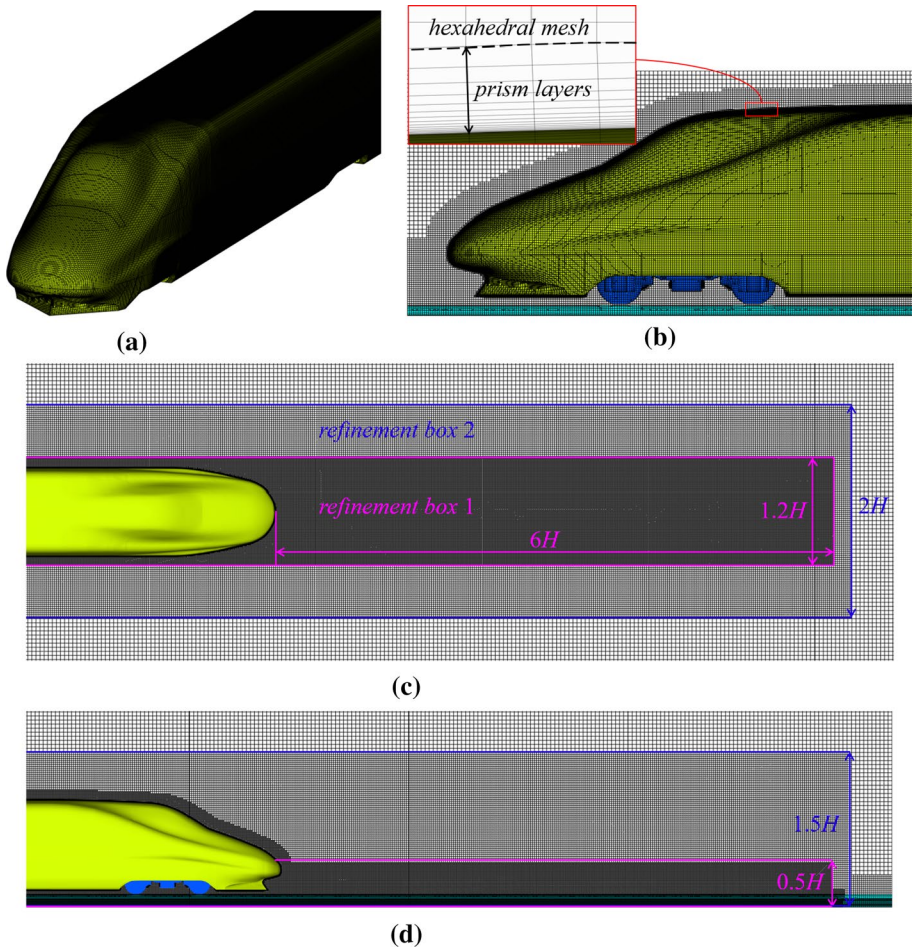
$$C_d = F_d/(0.5\rho U_{ref}^2 S) \tag{1}$$

Fig. 4 Configuration of the medium computational mesh: **a** mesh distribution on the HST surface and STBR, **b** prism layers around the HST. Description of the refinement boxes: **c** side view, and **d** top view. Magenta box: the first refinement box, blue box: the second refinement box

Table 2 Details of the computational meshes

Grids	n^+_{mean}	n^+_{max}	Δs^+_{mean}	Δs^+_{max}	Δl^+_{mean}	Δl^+_{max}	Size
Coarse	< 1.0	2.3	< 190	360	< 190	360	32 million
Medium	< 1.0	2.3	< 130	250	< 130	250	58 million
Fine	< 1.0	2.3	< 100	180	< 100	180	80 million

where F_d is the aerodynamic drag force. C_d is the aerodynamic drag coefficient. ρ is the constant air density (taken as 1.225 kg/m^{3-}). U_{ref} is the incoming flow speed, which is set as 60 m/s. S is the reference area, and $S = 0.175$ m^2.

It can be seen from Table 3 that drag coefficients of head, $C_{d\text{-car 1}}$, predicted by the coarse mesh shows a larger error compared to that obtained by the fine mesh, while the medium

Table 3 Comparison between experimental and numerical results

Method	Grids	$C_{d\text{-car }1}$
IDDES simulation (current study)	Coarse mesh (32 million)	0.138
	Medium mesh (58 million)	0.144
	Fine mesh (80 million)	0.145
Wind tunnel test (Zhang et al. 2018b)	–	0.145

mesh shows a good agreement with the fine case. The drag coefficients calculated by the current IDDES simulations are close to that obtained in the wind tunnel tests, and the maximum difference between the numerical results and the experimental data is less than 1% in both medium and fine grid cases. Thus, the medium mesh resolution and the current methodology is sufficient to obtain good prediction of aerodynamic drag of the HST.

Figure 5 compares the time-averaged slipstream velocity predicted by the coarse, medium and fine meshes along a line parallel to HST direction at the distance of 2 m from the centre of rail (COR) 1.4 m from the top of rail (TOR). The non-dimensional results of slipstream velocity U is defined by Eq. (2), in which u and v are the velocity components along the streamwise direction and spanwise direction, respectively. The time-averaged slipstream velocity predicted using the coarse mesh exhibits a larger deviation around the intermediate cars, while the medium resolution shows good agreement with the fine case, indicating an adequate mesh resolution of the medium mesh for the prediction of the slipstream. Combing with the mesh independence study on the aerodynamic drag and slipstream velocity, the medium mesh is found to have an adequate resolution and therefore will be used in all numerical simulations in the present study.

$$U = \frac{\sqrt{(U_{ref} - u)^2 + v^2}}{U_{ref}} \tag{2}$$

2.4 Numerical Method

In this study, the IDDES with Shear-Stress Transport k-ω turbulence model has been used to investigate the bogie position effects on the HST aerodynamics. This methodology
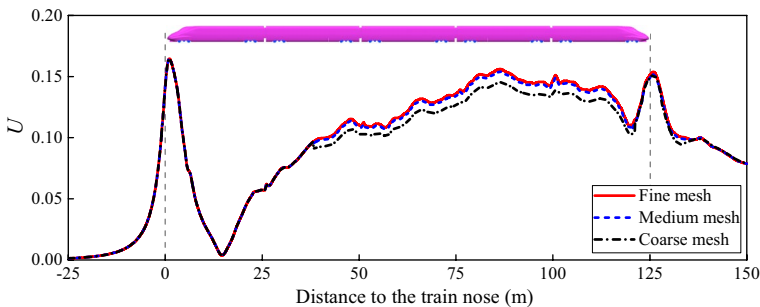

Fig. 5 Comparison of time-averaged slipstream velocity (U) along the streamwise sampling line located at 2 m from the COR and 1.4 m from the TOR predicted using different mesh resolutions

combines the advantages of the delayed detached eddy simulation (DDES) and the wall-modelled large eddy simulation (WMLES) (Shur et al. 2008). The DDES is derived from the DES method by introducing a delay function to prevent the LES method from being used in the boundary layer and to ensure that the Reynolds-averaged Navier–Stokes equations (RANS) are used to model the boundary layer. The present IDDES employs a modification of the length scale of the dissipation rate term in the turbulent kinetic energy transport equation of Menter's k-ω model (Menter 2012; Ghasemian and Nejat 2015). The length scale of the IDDES can effectively reduce the sub-grid viscosity in the log layer when compared to that of DDES. Furthermore, the WMLES model is designed to reduce the Reynolds number dependency and to allow the LES simulation of wall boundary layers at much higher Reynolds numbers than the standard LES models (Shur et al. 2008). As a typical hybrid turbulence model, the IDDES uses Reynolds-Averaged Navier–Stokes simulations (RANS) to simulate the boundary layer near the walls and utilizes the Large Eddy Simulation (LES) to capture the large-scale turbulent flow away from the walls. The comprehensive explanation and details of the IDDES method has been given by Spalart (2009). The IDDES method has been widely used in previous related studies, showing itself as a successful tool for HST flow predictions. Some examples consists in drag assessment (Niu et al. 2017; Wang et al. 2019a, 2020), slipstream prediction (Dong et al. 2020; Wang et al. 2018b, 2019b), underbody flow (Xia et al. 2017a; Wang et al. 2018a; Dong et al. 2019a), wake flow analysis (Xia et al. 2017b; Zhou et al. 2019; Chen et al. 2019; Li et al. 2019) and aeroacoustic prediction (Minelli et al. 2020).

The governing equations were solved using the commercial finite-volume CFD software ANSYS FLUENT. The Finite Volume Method (FVM) based on cell centres was adopted for the discretization of the controlling equations. Simulations were performed using a pressure-based solver. The SIMPLE (Semi-Implicit Method for Pressure-Linked Equations) algorithm was used to update the pressure and velocity fields. The bounded central differencing scheme and the second-order upwind scheme were used to solve the momentum equation and the k-ω equations, respectively. The second-order implicit scheme was used for the temporal advancement. The time derivative is discretized using the bounded second-order implicit scheme for unsteady flow calculations. The physical time step $\Delta t = 5 \times 10^{-5}$ s. The CFL number was less than 1.0 in more than 99% of the computational cells during the entire simulations, with the maximum value of 3.0. All the cases were initially run for a non-dimensional time $t^* = t U_{ref}/H = 60$ to make the flow fully developed, as shown in Fig. 6. After that, the averaging of the flow variables was initiated for the purpose of obtaining the flow statistics. The computational cost is also provided herein, which might be of interest to vehicle engineers when conducting a CFD analysis on train aerodynamics. All of the numerical simulations were performed using Intel-Xeon E5-2699 processors (2.40 GHz). The computational cost of each case is approximately 38,000 CPU hours.

2.5 Numerical Validation

To validate the accuracy of the current numerical method for predicting the aerodynamic drag, surface pressure distribution and slipstream of HSTs, the IDDES results are compared with the results from wind tunnel tests, full-scale field tests and reduced-scale moving-model tests, to make the numerical investigations more convincing. Firstly, the drag coefficient and surface pressure distribution on the upper centerline of the head car are compared with the experimental results measured by Zhang et al. (2018b) in a 8 m × 6 m

Fig. 6 Time history curves of $C_{d\text{-car }1}$, $C_{d\text{-car }2}$, $C_{d\text{-car }3}$, $C_{d\text{-car }4}$ and $C_{d\text{-car }5}$ in the original case (Case 1)
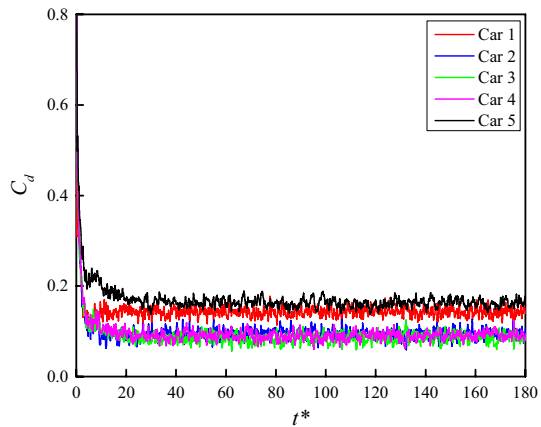
wind tunnel of the China Aerodynamics Research and Development Center. The wind tunnel setup and other experimental details can be found in Zhang et al. (2018b). Then, the comparison of the slipstream pressure between IDDES results and full-scale test results is done. The full-scale field tests were conducted on the Wuhan-Guangzhou high-speed railway line in China. The slipstream velocity distribution at the trackside position of an ICE3 HST predicted by the current numerical method is also compared with the existing reduced-scale moving model experimental data measured at the German aerospace center DLR (Bell et al. 2015). Note that two kinds of ground conditions are adopted in this section. For validating the IDDES results against the wind tunnel test results, the stationary STBR and ground were used. While the STBR and ground were set as moving walls with the same speed applied at the inlet when the IDDES results are compared to the full-scale field tests and the reduced-scale moving model tests.

2.5.1 Aerodynamic Force

Table 3 presents a comparison of the drag force obtained from the current numerical simulation and previous wind tunnel tests (Zhang et al. 2018b). The drag coefficients of car 1, $C_{d\text{-car }1}$, calculated by numerical simulations are close to that obtained in the wind tunnel tests, and the maximum difference between the numerical and experimental results is less than 1% in both medium and fine grid cases. Moreover, the values of the drag coefficients of the head car from the simulations conducted on medium and fine grids are close to previous numerical results (Zhang et al. 2018a). Thus, the present numerical resolution of the mesh and methodology is sufficient to obtain a good prediction of aerodynamic drag.

2.5.2 Surface Pressure Distribution

Figure 7 compares the distribution of pressure coefficients along the upper centerline line of the head car between the numerical results predicted using the medium mesh and the experimental data. The pressure coefficients C_p is defined by Eq. (3), where P is the time-averaged surface pressure and P_∞ is the static pressure of the wind tunnel test section. Generally, the numerical results are in good agreement with the experimental data, except for the positions where the curvature varies abruptly. Thus, the present numerical method and

Fig. 7 Comparison of time-averaged pressure coefficients (C_p) along the upper centerline on the roof of the head car of the original case (Case 1) between the wind tunnel experimental data and the present numerical simulation
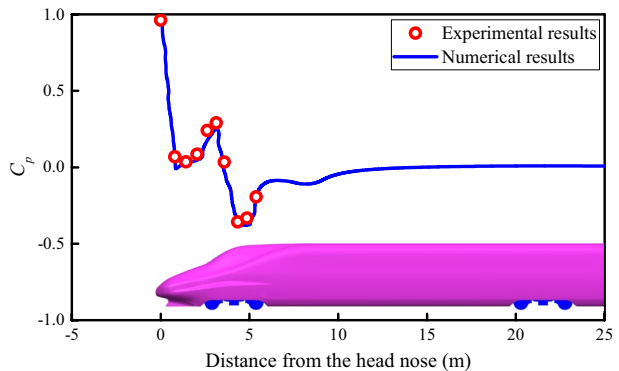
medium mesh resolution is sufficient to obtain an accurate prediction of the pressure distribution of the HST.

$$C_p = \frac{P - P_\infty}{0.5\rho U_{ref}^2} \tag{3}$$

2.5.3 Slipstream Pressure

To validate the accuracy of the current IDDES method for the prediction of the slipstream pressure around the HST, the numerical results are validated against the full-scale field test data. The full-scale field tests were conducted on the Wuhan-Guangzhou high-speed railway line by the Chinese Academy of Railway Science and Central South University. Figure 8 presents experimental instruments and their installation position. The pressure sensor was placed on the gravity centre of a human dummy, located at a distance of 3.15 m from the COR and 1.4 m from the TOR. The speed of the passing full-scale CRH2 HST was 350 km/h, yielding a high Reynolds number of Re=2.4×10^7. Previous studies have shown that the results do not change significantly with increasing Reynolds number if the Reynolds number exceeds the critical value of 3×10^5 (Sterling et al. 2008; Hemida and Krajnovic 2010; Zhang et al. 2017). The Reynolds number in the full-scale tests (2.4×10^7) and numerical simulation (1.85×10^6) are far greater than this critical value, and therefore the full-scaled test results are used to validate the accuracy of the present numerical predictions.

Figure 9 shows the comparison of pressure coefficients distribution obtained from IDDES simulation and the full-scale field test. The streamwise monitoring line in the IDDES simulation is located at the position of 1.4 m from TOR and 3.15 m from COR, and the installation position of pressure sensor is shown in Fig. 8. In the full-scale test, the CRH2 HST consisted of eight cars, while only five cars were used in the IDDES simulation with the aim to reduce the computational cost. This leads to an equivalent gap to three intermediate cars in the numerical results in Fig. 9. It should be noted that pressure coefficients measured in the full-scale experiment are the instantaneous value, while the one predicted by IDDES are time-averaged results. It can be seen from the comparison in Fig. 9 that the numerical results are close to the experimental results. In particular, the peak-to-peak value of pressure coefficients caused by the passing of the head and the tail
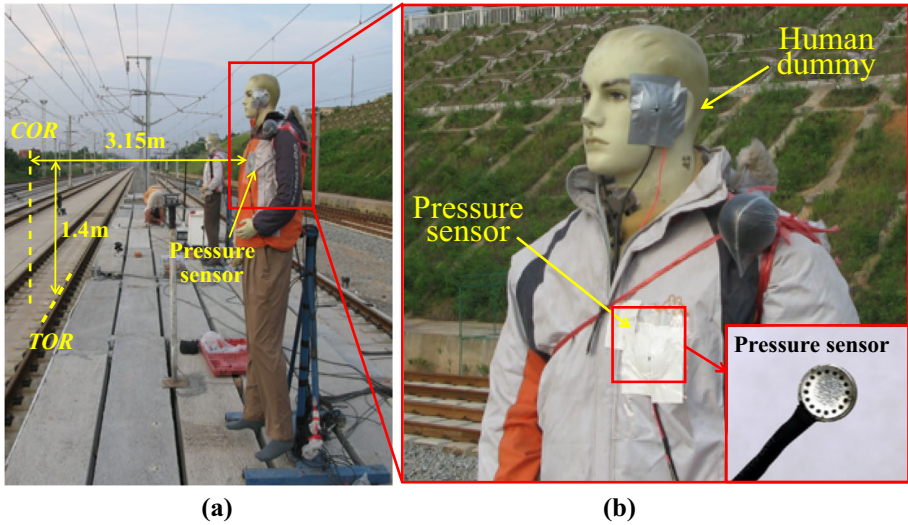
Fig. 8 Instruments and their installation in the full-scale field test: **a** installation positions of the instruments; and **b** details of the pressure sensor and the human dummy
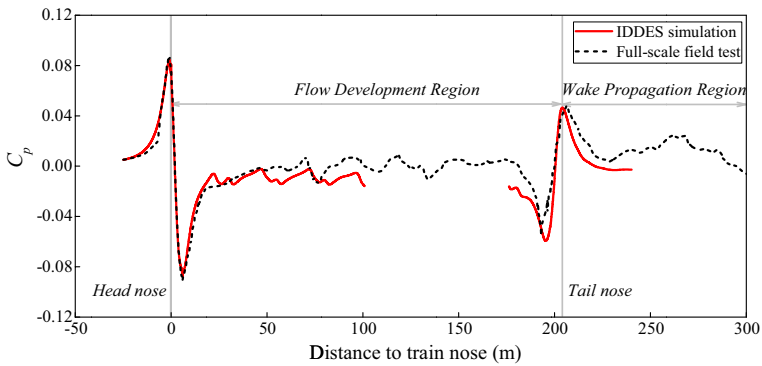

Fig. 9 Comparison of time-averaged pressure coefficients (C_p) calculated by IDDES simulation and instantaneous C_p measured in full-scale field test. The sampling line locates at the distance of 1.4 m from TOR and 3.15 m from COR

cars differs less than 2%, indicating an accurate prediction of the slipstream pressure distribution of the current numerical method.

2.5.4 Slipstream Velocity

In order to validate the slipstream prediction against available experimental data, the same meshing technique with medium resolution and the numerical method is used on an ICE3 HST. The geometry models of ICE3 HST used in the reduced-scale moving model tests and numerical simulation are presented in Fig. 10. The scale ratio of the ICE3 HST is 0.125, and its height is $h = 0.485$ m and the total length (l) and width (w) are $l = 19.73\,h$ and
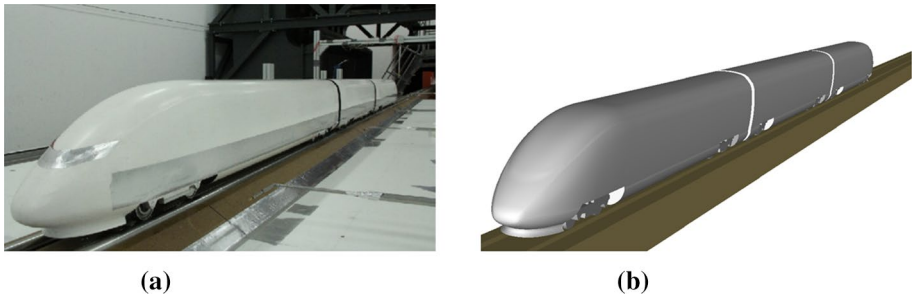
Fig. 10 ICE3 HST geometry model used for the validation of the slipstream velocity: **a** taken from the reduced-scale moving model tests (Bell et al. 2015), and **b** taken from the numerical simulation
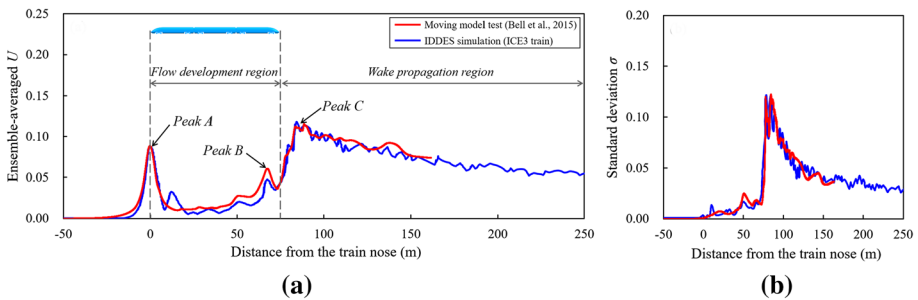

Fig. 11 Comparison of ensemble-averaged slipstream velocity U and standard deviation σ at the trackside position between the current IDDES simulation and reduced-scale moving model test: **a** ensemble-averaged slipstream velocity U, and **b** standard deviation σ

$w = 0.76\,h$, respectively. The ensemble-averaged slipstream velocity and standard deviation at the trackside measurement position beside the ICE3 HST are compared with the existing data from reduced-scale moving model tests (Bell et al. 2015) at the same Reynolds number (Re $= 3.3 \times 10^5$). The moving model tests were carried out at the German aerospace center DLR, and more detailed experimental information has been provided in Bell et al. (2015). Additionally, the distance from the nose of head car presented in Fig. 11 is given at full-scale in both numerical and experimental data.

As seen from the reduced-scale moving model test data in Fig. 11a, the slipstream velocity at the trackside position increases rapidly and forms Peak A in the vicinity of the head car. This is followed by a sudden decrease and gradual growth of the velocity along the intermediate cars in the *Flow development region*. The value of the slipstream velocity increases rapidly again at the streamlined part of the tail car and contributes to Peak B. In the *wake propagation region*, the slipstream velocity increases as expected and then attenuates with the increasing distance from the tail nose, resulting in Peak C in the near wake region. Figure 11a shows that the IDDES simulation closely captures the Peak A located at the head car, Peak B around the tail car and Peak C in the near wake region. Besides, the IDDES simulation also accurately captures the gradual increasing trend of the slipstream velocity in the *Flow development region* and a similar attenuation trend, downstream of Peak C, in the *Wake propagation region*. In particular, the value of Peak A predicted by the IDDES simulation shows less than 1% difference as compared to the experimental results,

indicating an accurate prediction of slipstream distributions in the current numerical simulation. Additionally, in Fig. 11b the IDDES simulation presents a highly similar trend of slipstream standard deviation, at the trackside position, compared to the reduced-scale moving model experimental results. In conclusion, the overall good agreements with the wind tunnel test (aerodynamic drag and surface pressure coefficient), the full-scale field test (slipstream pressure) and reduced-scale moving model test (slipstream velocity) allow us to select the current numerical method and medium mesh resolution to investigate the bogie position effects on the aerodynamic behavior of the CRH2 HST.

3 Results and Discussion

3.1 The Instantaneous Flow Structures

To provide an intuitive understanding of the bogie position on the flow characteristics around the HST, the instantaneous vortex structures around the HST are qualitatively compared for three cases, using the iso-surfaces of the second invariant of the velocity gradient for $Q = 60,000$, colored by the slipstream velocity U in Fig. 12. Figure 12 shows that the distribution of the vortices around bogie 1 and near the wake region in three cases are clearly different, indicating the dominant effect of the positions of the first and last bogie on the local flow structures. As highlighted by $C1$ in Fig. 12, Case 1 has a higher flow range of the vortices generated near bogie 1, along the vertical direction, than that in Case 2 and Case 3, and the scale of the vortices in Case 1 are significantly larger than that in Case 2, while Case 3 shows the smallest. Previous studies (Zhang et al. 2018a; Wang et al. 2019b) have found that the velocity of the underbody flow decreases along the flow direction. Case 1 and Case 3 have the shortest and longest distance between the front cowcatcher tip and the first bogie, respectively, resulting in the highest and lowest velocity distribution around bogie 1. The airflow with higher speed in Case 1 directly impacts on the windward surface of the first bogie and the rear plate of the bogie cavity, generating more turbulent local flow structures, as shown in $C1$. Another observation in Fig. 12 is that Case 1 shows the most turbulent flow in the near wake region, where the wake vortices in Case 1 are turned up while they tend to be closer to the STBR in Case 2 and Case 3. Moreover,
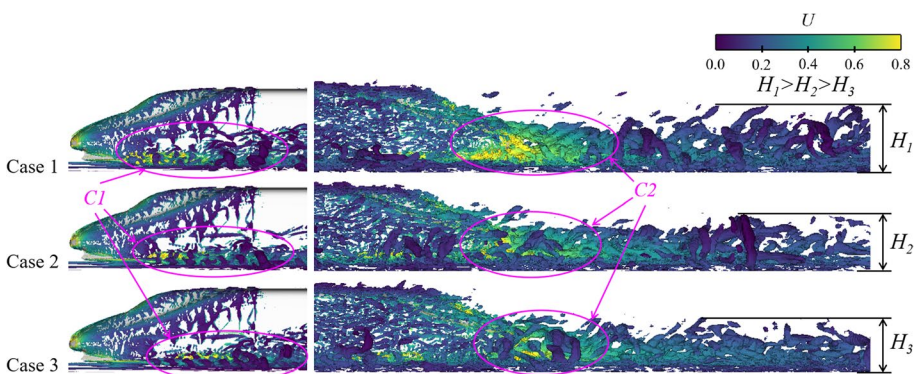

Fig. 12 Instantaneous flow structures around the HST. Iso-surfaces of the second invariant of the velocity $Q = 60,000$ colored by the time-averaged slipstream velocity

the height of the wake flow in Case 1 is the highest and Case 3 shows the lowest wake vortices. Furthermore, Case 1 and Case 3 have the highest and lowest, respectively, slipstream velocity distribution in the near wake region, showing the largest and smallest yellow area, as compared by *C2* in Fig. 12.

3.2 The Slipstream Velocity

In this paper, the time-averaged slipstream velocity and pressure distribution along the streamwise sampling lines will be discussed. In order to provide an intuitive understanding, all the measurement positions of the streamwise sampling lines are presented in full scale, see in Fig. 13.

Figure 14 compares the time-averaged slipstream velocity at various distance from the COR at the trackside and platform heights. In this figure, the maximum values of the slipstream velocity are highlighted for further comparison. The general observation in Fig. 14 is that a sharp peak of time-averaged slipstream velocity occurs near the head nose. After that, the time-averaged slipstream velocity decreases sharply followed by a gradual recovery along the HST direction, similar to that reported by Guo et al. (2018) and Li et al. (2019). This can be ascribed with the boundary layer distribution around the HST, as shown in Fig. 15, in which the thickness of boundary layer at both trackside and platform height grows along the HST length direction. The thicker boundary layer will determine a higher velocity of the slipstream around the HST (Xia et al. 2017). In Fig. 15, Case 1 shows the thickest boundary layer distribution, while it becomes thinnest in Case 3. This explains the highest slipstream velocity in Case 1 and the lowest in Case 3. The values of time-averaged slipstream velocity at both trackside and platform heights decrease with increasing distance from COR. Compared with the distribution of slipstream velocity at

Fig. 13 Positions of streamwise monitoring lines of slipstream velocity and pressure distribution around the HST. Hollow pink circle: the trackside position; hollow pink square: platform position, proposed by TSI (TSI HSRST 2008)
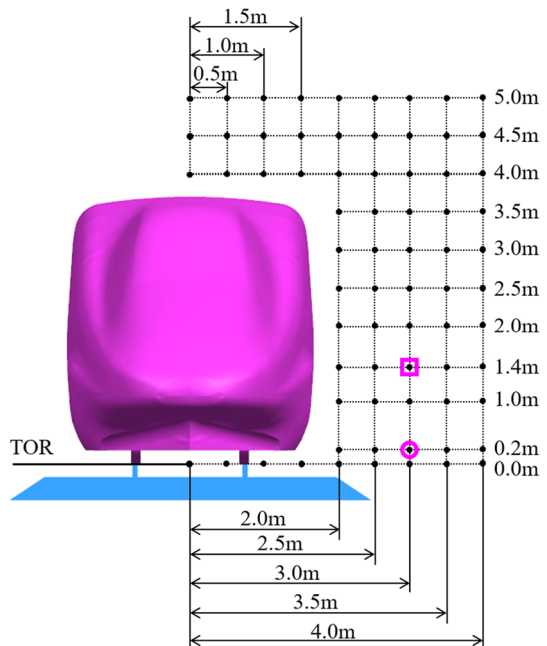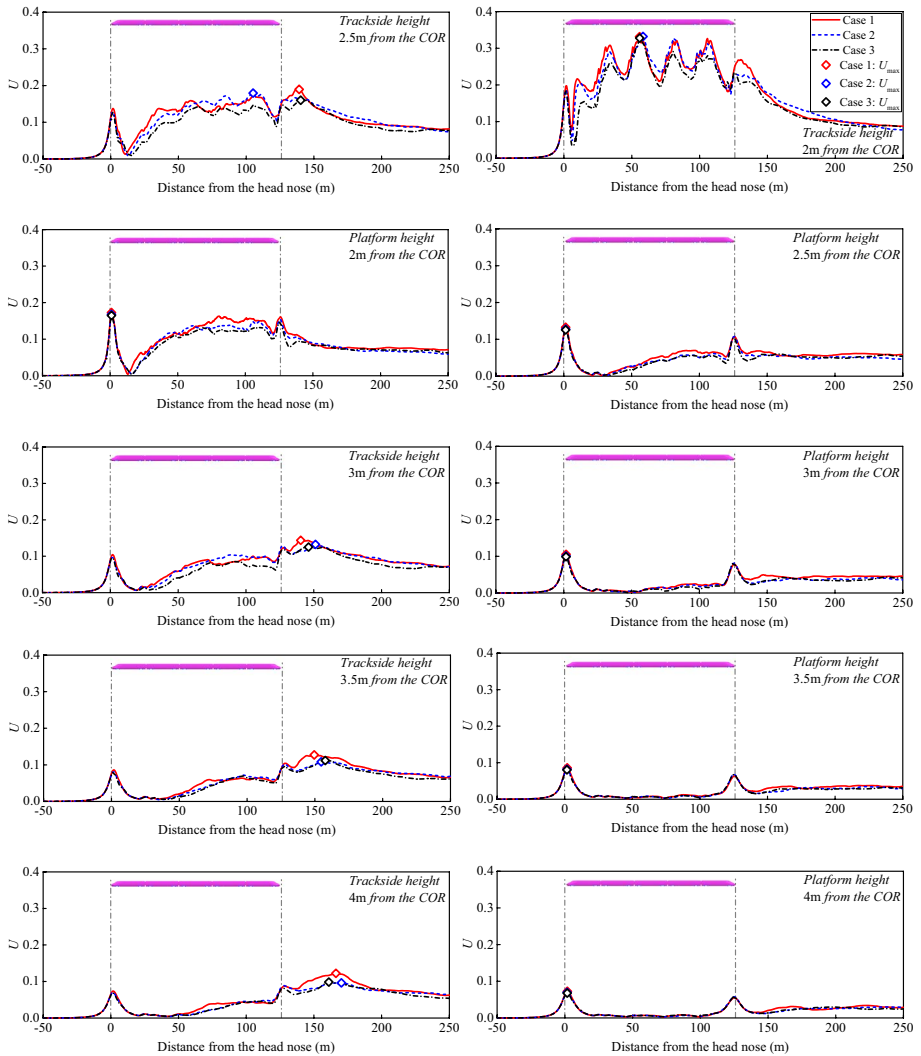
Fig. 14 Comparison of the time-averaged slipstream velocity distribution along the streamwise sampling lines located at a distance of 2.0 m, 2.5 m, 3.0 m, 3.5 m and 4.0 m from the COR at the trackside height (left side) and the platform height (right side)

platform height, the trackside data shows a more complex plot due to the complexity of the bogie. Moreover, the values of slipstream velocity at trackside height are much higher than that at platform height, due to the thicker boundary layer distribution observed near the tracks in Fig. 15. For the same distance from COR, the difference of the slipstream velocity between three cases at trackside height are larger than that at platform height, indicating a larger influence of the bogie position on the lower flow field of the HST. Additionally, the difference of the boundary layer thickness for three cases also indicates a dominant effect of the bogie position on the aerodynamic drag of the HST, which will be further discussed in Sect. 3.5.
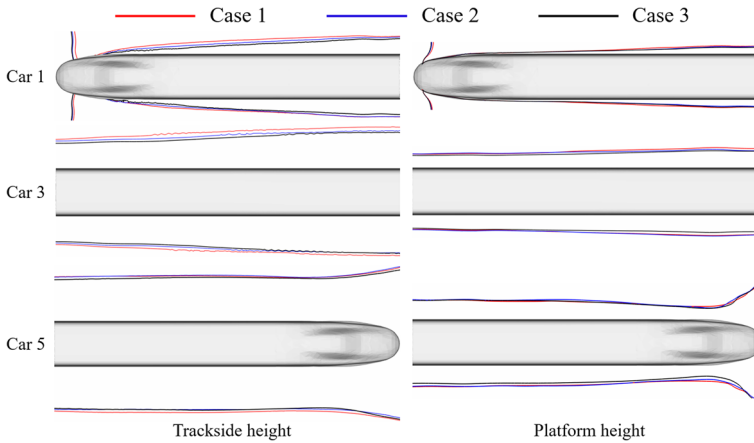
Fig. 15 Comparison of boundary layer thickness distribution around the HST on the horizontal planes located at trackside height and platform height between three cases

To provide a more quantitative analysis of the maximum slipstream velocity distribution at trackside and platform heights, the maximum values of the slipstream velocity (U_{max}) on the streamwise sampling lines are compared. The positions of the streamwise sampling lines are highlighted in Fig. 14. Figure 16 shows that the maximum values at both trackside and platform heights decrease with the increasing distance from the COR. The differences of the maximum values at trackside height are clearer than those at platform height. Furthermore, compared to the maximum value of the slipstream velocity at trackside position (3 m from the COR and 0.2 m from the TOR) in Case 1, it decreases by 7.86% in Case 2 and 12.86% in Case 3. The corresponding figures for the platform position (3 m from the COR and 1.4 m from the TOR) are 4.36% in Case 2 and 6.18% in Case 3. This indicates the clear influence of the bogie position on the maximum slipstream velocity at both trackside position and platform position. The downstream movement of the first bogie is found to effectively reduce the maximum slipstream velocity at two TSI monitoring positions. Figure 17 compares the time-averaged slipstream velocity at the distance of 3 m from the
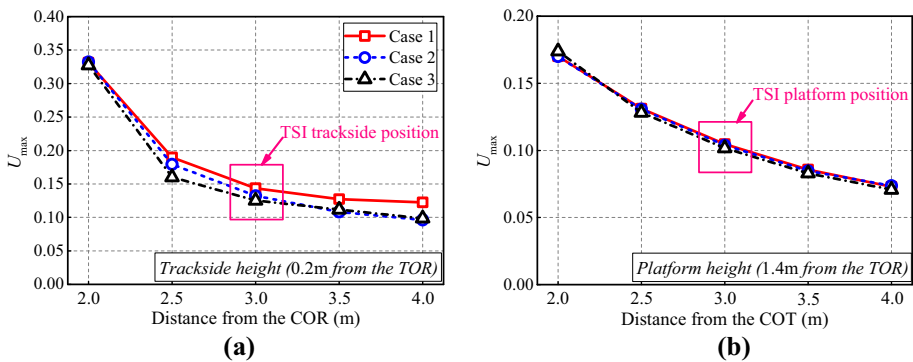

Fig. 16 Comparison of the maximum values of the slipstream velocity at trackside and platform heights for the considered cases: **a** trackside height, and **b** platform height

COR and at different distances from the TOR between three cases. It shows that Case 1 has the highest slipstream velocity while U is the lowest in Case 3. With the increase of the distance from TOR, the value of the slipstream velocity in three cases decreases clearly, and the difference of the slipstream velocity caused by the bogie position becomes less obvious, and it can be neglected as the distance from TOR exceeds 2 m. This confirms that the bogie positions primarily alter the flow structures around the lower part of the HST.

In order to investigate the influence of the positions of the first and last bogies on the distribution of maximum value of the slipstream velocity around the HST in the whole computational domain, the contour of the ratios of U_{max} of Case 2 and Case 3 to U_{max} of Case 1 are plotted in Fig. 18. The ratio of Case 2 to Case 1, R_{v-1}, is defined by Eq. (4), and ratio of Case 3 to Case 1, R_{v-2}, is defined by Eq. (5).

$$R_{v-1} = \frac{U_{\mathrm{max-case\,2}}}{U_{\mathrm{max-case\,1}}} \tag{4}$$

$$R_{v-2} = \frac{U_{\mathrm{max-case\,3}}}{U_{\mathrm{max-case\,1}}} \tag{5}$$

where $U_{\mathrm{max-case\,1}}$, $U_{\mathrm{max-case\,2}}$ and $U_{\mathrm{max-case\,3}}$ are the maximum values of time-averaged slipstream velocity along the streamwise sampling lines presented in Fig. 13 in the whole computational domain in three cases. Note that the maximum values used for plotting the contour might occur at different distance from the head nose.

The general findings in Fig. 18 are that the maximum values of the slipstream velocity around the HST decrease significantly in Case 2 and Case 3, and the distribution of R_{v-2} in the whole domain has a lower value than that of R_{v-1}. This means that the positions of
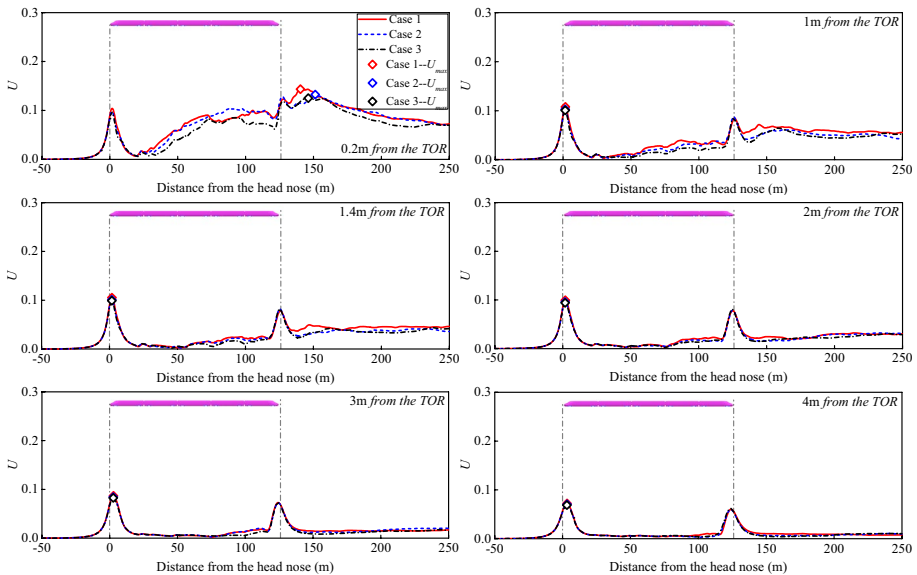

Fig. 17 Comparison of time-averaged slipstream velocity distribution for three cases along the sampling lines with a distance of 0.2 m, 1.0 m, 1.4 m, 2.0 m, 3.0 m and 4.0 m from the TOR at the distance of 3 m from the COR
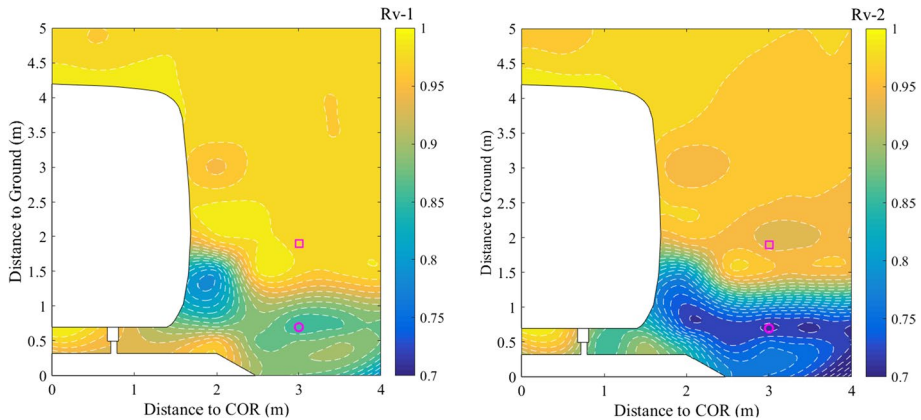
Fig. 18 Comparison of the distribution characteristics of the maximum values of the slipstream velocity along the sampling lines near the HST between different cases. (Hollow pink circle: the trackside position; hollow pink square: platform position)

the first and last bogie play a dominant role on the distribution of the maximum values of the slipstream velocity around the HST, and the maximum values can be decreased significantly by moving downstream the first bogie and upstream the last bogie. Besides, the maximum values at the trackside positions in Case 3 is far lower than that in Case 2, while the this is not obvious at the platform position, indicating that the bogie position primarily affects the distribution characteristics of the maximum value near the lower parts of the HST. The maximum value in Case 3, from ground to the platform position within the distance of 2 m from the COR, are much lower than that in cases 1 and 2, which suggests that Case 3 provides greater security for the trackside workers as the HST passes by. This effect can be neglected for the passengers standing on the platform. Overall, the maximum values of the time-averaged slipstream velocity can be decreased significantly and safety of trackside workers would be significantly improved if the first bogie and last bogie are moved toward the HST center. These effects becomes more significant with increasing distance of the bogies from the train noses.

3.3 The Slipstream Pressure

Previous studies (Baker et al. 2014a, b; Bell et al. 2014, 2015) have found that the time-averaged pressure coefficient increases sharply as the head car passes by. The pressure coefficient is defined as $C_p = \frac{P - P_\infty}{0.5 \rho U_{ref}^2}$, where P is the time-averaged pressure distribution and P_∞ is the reference pressure. Then, the C_p value decreases rapidly due to the acceleration effect brought by the streamline shape of the head car on the local airflow. After that, the second sharp peak of time-averaged pressure occurs near the tail car and the peak-to-peak values of the pressure coefficient ($C_{p\_peak-to-peak}$) around the head car are far higher than that near the tail car. Thus, Fig. 19 presents the comparison of the peak-to-peak pressure values at the head car for three cases at the trackside and platform heights among three cases. It shows that peak-to-peak values near the head car at two heights decrease with increasing distance from the COR, and the differences between peak-to-peak values at the trackside height are obviously higher than that at the platform height.
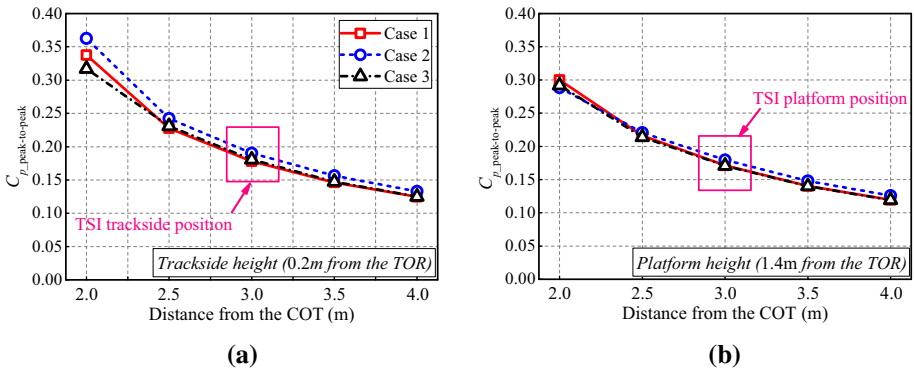
Fig. 19 Comparison of the peak-to-peak pressure values at trackside and platform heights for the considered cases: **a** trackside height, and **b** platform height

The peak-to-peak values around the head car at both trackside height and platform height decrease significantly in Case 2 and Case 3, when compared to that in Case 1. Furthermore, the downstream movement of the first bogie in Case 3 shows a larger reduction of the peak-to-peak value than that of Case 2. In particular, compared to the peak-to-peak pressure value at trackside position in Case 1, it decreases by 8.32% and 9.86% in Case 2 and Case 3, respectively. The corresponding values for the platform position are 5.62% in Case 2 and 7.72% in Case 3.

In order to better identify the influence of the positions of the first and the last bogie on the distribution of the maximum value of the pressure around the HST, the maximum pressure values in Case 2 ($C_{p\ \text{max-case 2}}$) and Case 3 ($C_{p\ \text{max-case 3}}$) are normalized by the value obtained in Case 1 ($C_{p\ \text{max-case 1}}$). The obtained results are presented in Fig. 20. The non-dimensional maximum pressure coefficients in Case 2 (R_{p-1}) and Case 3 (R_{p-2}) are defined by Eqs. (6) and (7).
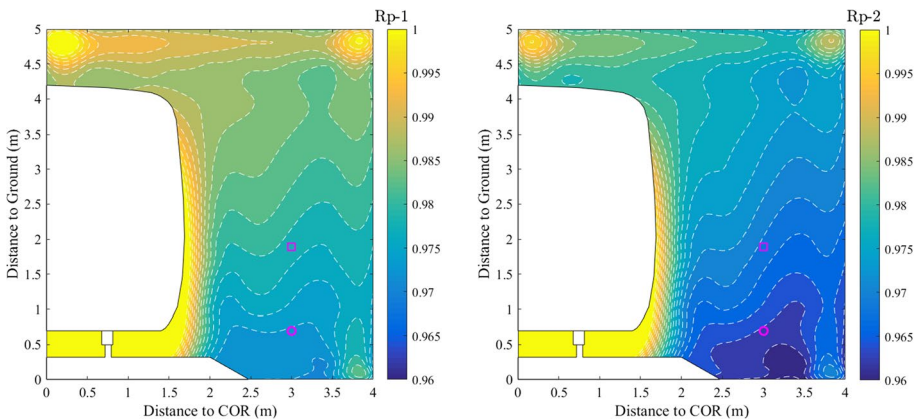

Fig. 20 Comparison of the maximum values of pressure coefficients along the sampling lines near the HST in the domain between different cases. (Hollow pink circle: the trackside position; hollow pink square: platform position)

Fig. 21 Time-averaged slipstream velocity in the near wake region of the HST: **a** slipstream velocity distri- ▶ bution on the vertical planes located at a distance of $x=1H$, $x=2H$ and $x=3H$ from the tail nose; **b** comparison of slipstream distribution on vertical planes between three cases; **c** slipstream velocity distribution on the horizontal planes at the trackside and platform height; and **d** comparison of slipstream velocity distribution on the horizontal planes. The red solid line: Case 1; blue solid line: Case 2; black solid line: Case 3

$$R_{p-1} = \frac{C_{p\max-\text{case } 2}}{C_{p\max-\text{case } 1}} \tag{6}$$

$$R_{p-2} = \frac{C_{p\max-case\,3}}{C_{p\max-case1}} \tag{7}$$

where $C_{p\max\text{-case 1}}$, $C_{p\max\text{-case 2}}$ and $C_{p\max\text{-case 3}}$ are the maximum value of time-averaged slipstream pressure coefficients along the horizontal measurement lines parallel to the HST length direction in the three cases.

Figure 20 shows that the maximum values of time-averaged pressure around the HST in Case 2 and Case 3 decrease significantly compared to that in Case 1, especially for Case 3 where the bogies are the farther from the nose tips. The maximum values of pressure at two TSI positions in Case 3 are lower than that in Case 1 and Case 2. Similar to the observation done for Fig. 18, the movement of the first and last bogie primarily lowers the maximum pressure value around the HST at lower position. In addition, with bogie farther away from the noses a better aerodynamic performance is observed, in terms of improving the safety level of the trackside workers.

3.4 The Wake Flow

Figure 21 presents the distribution characteristics of the time-averaged slipstream velocity in the near wake region. The general observation from Fig. 21a is that the high-speed slipstream mainly distributes within the HST's width range in the spanwise direction from the top of the ballast to the tail nose in the vertical direction. The value of the slipstream velocity decreases clearly with an increasing distance from the tail nose. Figure 21b compares the time-averaged slipstream velocity at vertical planes between three cases. Here Case 1 and Case 3 shows the highest and lowest value of the slipstream velocity. Furthermore, the time-averaged slipstream velocity on the horizontal planes at trackside and platform heights are presented in Fig. 21c. The value of the slipstream velocity in the near wake region at trackside height is much higher than that at platform height. For the comparison of the slipstream velocity in the near wake region at both the trackside and the platform heights, Case 2 and Case 3 show the lower value of slipstream velocity distribution compared to Case 1. In addition, the differences in the slipstream velocity distribution between various cases are obvious, with cases 1 and 3, having the largest and the smallest yellow area, respectively. Thus, the upstream movement of the last bogie can effectively reduce the slipstream velocity in the near wake region.

Figure 22 depicts the time-averaged velocity streamlines projected on the vertical planes located at $x=1H$, $x=2H$ and $x=3H$ from the tail nose. These planes are colored by the dimensionless streamwise vorticity concentration ($\omega_x^+ = \omega_x \cdot H/U_{inf}$). A pair of strong rotating vortices (vortex A_l and vortex A_r) behind the HST is clearly observed in Fig. 22, accompanied with a pair of small-scale vortices near the track (vortex B_l and vortex B_r). In general, the size of vortex A becomes larger with increasing distance from the tail nose.
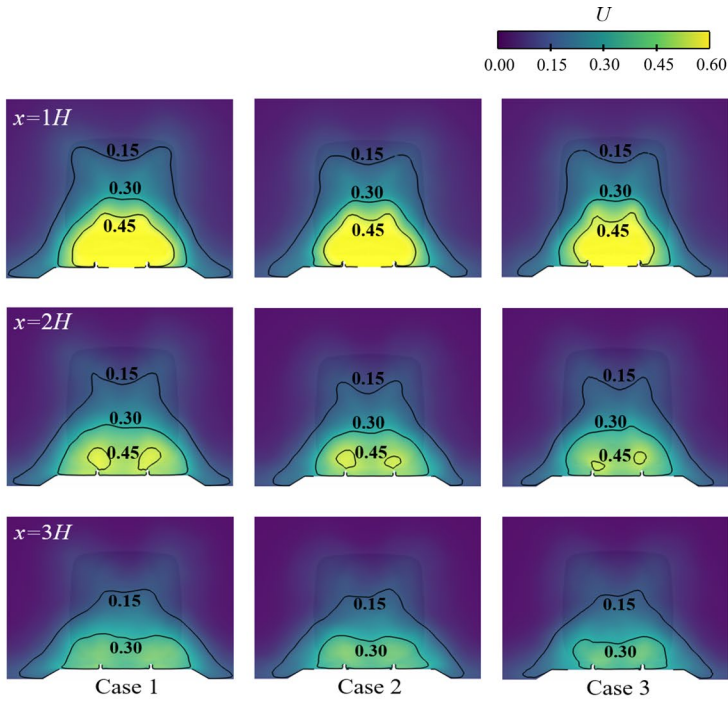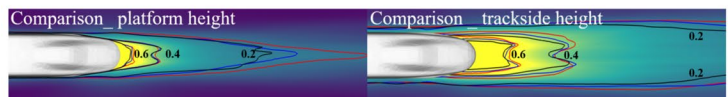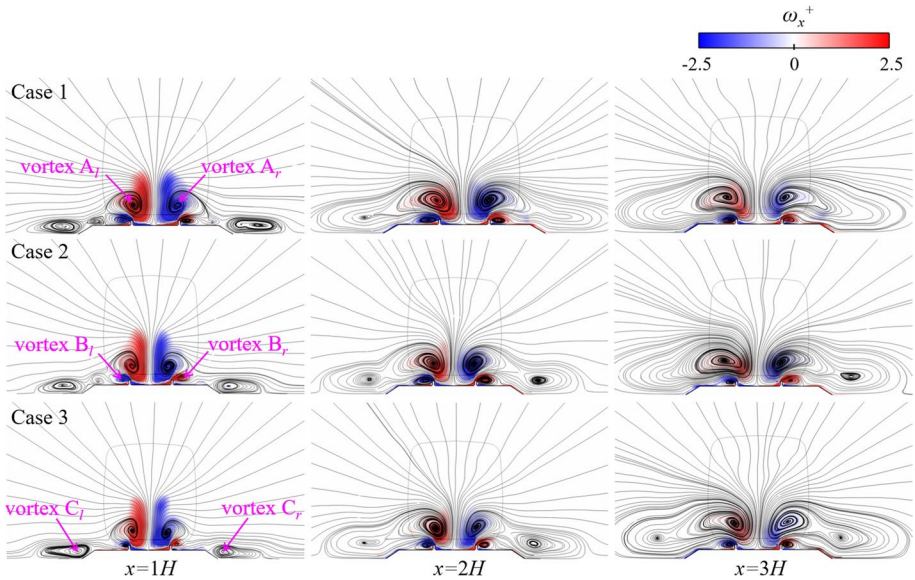
(a)
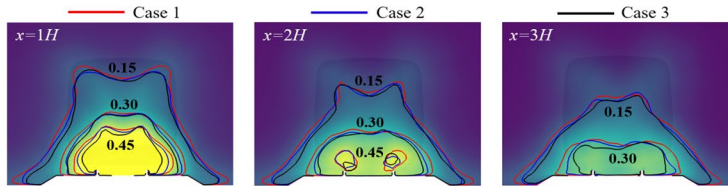
(b)
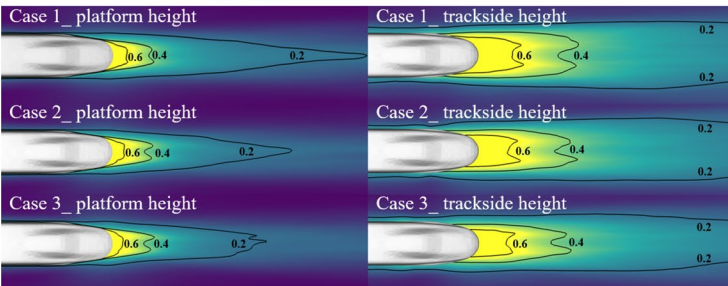
(c)

(d)

Fig. 22 Comparison of longitudinal vortex structures between three cases on the vertical planes located at a distance of $x=1\,H$, $x=2\,H$ and $x=3\,H$ from the tail nose

Furthermore, vortex C_l and vortex C_r appear near the STBR at a distance $x=1H$ from the tail nose and it grows larger with increasing distance from the tail nose, eventually merging into vortices A_l and A_r. The size of the large-scale longitudinal vortices A_l and A_r in Case 1 is slightly larger than that in Case 2 and Case 3, while this difference shows less obvious with increasing distance between the vertical planes and the tail nose. Moreover, the span-wise distance between vortex cores of A_l and A_r in Case 1 is the longest, and Case 3 has the shortest, indicating a narrower longitudinal vortex with an upstream movement of the last bogie. This also well explains the small area with high-speed slipstream velocity that Case 3 presents, especially in the spanwise direction, as shown in Fig. 21b. This is because the longitudinal vortex structure drives a low-momentum airflow, accompanied with a high slipstream velocity, which flows outwards from the wake center (Bell et al. 2014; Xia et al. 2017). The narrow longitudinal vortices in Case 3 contribute to the lowest slipstream velocity distribution in the near wake region, when compared with that in Case 1 and Case 2. Additionally, the upstream movement of the last bogie can effectively decrease the size of large-scale longitudinal vortices and thereby contribute to a lower pressure drag (Wang et al. 2018a, 2019a, 2020; Dong et al. 2020), which will be further compared in Sect. 3.5.

3.5 The Aerodynamic Drag

According to the results presented so far, the movement of the first and the last bogies toward the HST center in the streamwise direction, significantly affect the boundary layer thickness and the size of the longitudinal vortex structure, which also indicates a dominant influence on both the viscous and the pressure drag of the HST (Dong et al. 2020; Wang et al. 2019a, 2020). Thus, in this section, the comparison of the aerodynamic drag of each car between three cases is conducted. As shown in Fig. 23, the

Fig. 23 Comparison of the aerodynamic drag values of each car of the HST between three cases
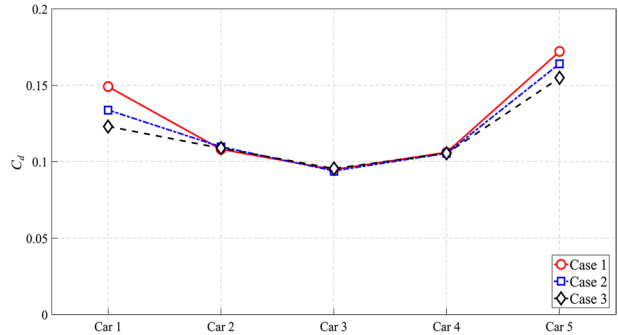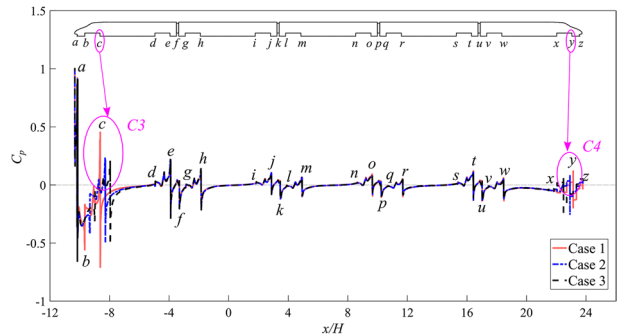

Fig. 24 Comparison of the time-averaged pressure distribution along the bottom centerline of the HST between three cases. *C3*: comparison of the positive pressure distribution on the rear plates of the first bogie cavity; *C4*: comparison of the positive pressure distribution on the rear plates of the last bogie cavity

movement of the first and last bogies is found to have more influence on reducing the drag values of the head and tail cars, while a lower effect is observed on the intermediate cars. In particular, compared to Case 1, the drag values of the head and tail cars decrease by 10.26% and 4.64% in Case 2, while Case 3 shows a 17.46% and 10.05% drag reduction. This is because the rear plates of the first and last bogie cavities in Case 2 and Case 3 experience a weaker impinging airflow and thereby present a clear lower positive pressure distribution, as shown by the peak values highlighted by *C3* and *C4* in Fig. 24. This significantly decreases the drag value of the HST (Wang et al. 2019a, 2020; Zhang et al. 2018a). Additionally, compared to the total drag value of the entire HST in Case 1, a 3.67% in Case 2 and 6.78% in Case 3 decrease is observed. Therefore, the movement of the first and last bogies is greatly beneficial for saving the energy consumption of a HST.

4 Conclusions

The influence of the position of the first and last bogie on the aerodynamic performance of a five-car grouped CRH2 HST has been studied using an improved delayed detached-eddy simulation (IDDES) at $Re = 1.85 \times 10^6$. The results of the numerical simulations have been validated against experimental data obtained from a previous wind tunnel test, a full-scale field test and a reduced-scale moving model test. The results are summarized as follows.

1. The movement of the first and last bogies toward the HST center is found to decrease the boundary layer thickness around the HST, thereby decreasing the time-averaged slipstream velocity distribution aside and behind the HST, especially at a lower position near the STBR. For trackside position, the maximum slipstream velocity obtained in Case 2 and Case 3 are 7.86% and 12.86% lower, respectively, than the corresponding value for Case 1. The bogie position also changes the distribution characteristics of the maximum value of the slipstream velocity in the whole domain.

2. The peak-to-peak pressure values occurring at the head car are significantly reduced with bogies placed farther from the nose tip, compared to the original case (Case 1). The upstream movement of the last bogie increases the peak-to-peak values near the tail car, especially for Case 3. For the same distances from the COR and the TOR, the peak-to-peak values near the tail car are anyway far lower than that near the head car. Comparing the maximum peak-to-peak pressure values at the trackside position, a 8.32% reduction in Case 2 and a 9.86% reduction in Case 3 are observed compared to Case 1, indicating a dominant effect of the first bogie movement. This improves the safety level of the trackside workers.

3. Compared to Case 1, Case 2 and Case 3 show better aerodynamic performance by achieving an overall 3.67% and 6.78% drag reduction for the HST. This is because the movement of the first and last bogies toward the HST center contributes to a smaller scale longitudinal vortex structure in the near wake region, less impingement on the rear plates of the cavities caused by the high-speed underbody flow and a thinner boundary layer distribution around the HST. More specifically, the movement of the first and last bogies toward the HST center, effectively decreases the drag values of the head and tail car, while a lower effect is observed on the intermediate cars. In particular, compared with the original HST model (Case 1), the drag values of the head and tail cars in Case 2 decrease by 10.26% and 4.64%, and the corresponding reduced drag values in Case 3 are 17.46% and 10.05%, respectively.

Overall, this study provides a significant result regarding the effect of the bogie positions, which not only shows a possible energy savings, but also a safety improvement, from a train aerodynamics point of view. This information would be considered for further applications and possibly integrated into the design of new HST models.

Note that for real HST, the Reynolds number is much higher than that in the present study. The turbulent incoming flow and detailed train's bottom geometries will contribute to the formation of more complex flow structures, especially in the underbody flow region. Although, the displacement of the first and last bogies towards the HST center contributes to better aerodynamics performance, its influence on the vehicle system dynamics, underbody equipment layout, snow accretion in the bogie regions and sand invasion in the equipment cabins are not discussed. These factors need to be accounted in the planned future investigations related to the influence of bogie position on the aerodynamic behaviours when, for example, a HST runs under strong crosswind.

Author Contributions JW: Data curation, Formal analysis, Writing—original draft. GM: Supervision, Writing—review & editing. XM: Investigation, Visualization. JZ: Methodology, Validation. TW: Writing—review & editing. GG: Project administration, Funding acquisition. SK: Resources, Software, Writing—review & editing.

Compliance with Ethical Standards

Conflict of interest We declare that we have no financial and personal relationships with other people or organizations that can inappropriately influence our work, there is no professional or other personal interest of any nature or kind in any product, service and/or company that could be construed as influencing the position presented in, or the review of, the manuscript entitled, "The effect of bogie positions on the aerodynamic behavior of a high-speed train. An IDDES study".

References

Baker, C.J., Dalley, S.J., Johnson, T., Quinn, A., Wright, N.G.: The slipstream and wake of a high-speed train. Proc. Inst. Mech. Eng. Part F. J. Rail Rapid Transp. **215**(2), 83–99 (2001)

Baker, C.J., Quinn, A., Sima, M., Hoefener, L., Licciardello, R.: Full-scale measurement and analysis of train slipstreams and wakes: Part 1: ensemble averages. Proc. Inst. Mech. Eng. Part F. J. Rail Rapid Transp. **228**(5), 451–467 (2014a)

Baker, C.J., Quinn, A., Sima, M., Hoefener, L., Licciardello, R.: Full-scale measurement and analysis of train slipstreams and wakes: Part 2: Gust analysis. Proc. Inst. Mech. Eng. Part F. J. Rail Rapid Transp. **228**(5), 468–480 (2014b)

Bell, J.R., Burton, D., Thompson, M., Herbst, A., Sheridan, J.: Wind tunnel analysis of the slipstream and wake of a high-speed train. J. Wind Eng. Ind. Aerodyn. **134**, 122–138 (2014)

Bell, J.R., Burton, D., Thompson, M., Herbst, A., Sheridan, J.: Moving model analysis of the slipstream and wake of a high-speed train. J. Wind Eng. Ind. Aerodyn. **136**, 127–137 (2015)

Bell, J.R., Burton, D., Thompson, M.C., Herbst, A.H., Sheridan, J.: The effect of tail geometry on the slipstream and unsteady wake structure of high-speed trains. Exp. Therm. Fluid Sci. **83**, 215–230 (2017)

Bell, J.R., Burton, D., Thompson, M.C., Herbst, A.H., Sheridan, J.: Flow topology and unsteady features of the wake of a generic high-speed train. J. Fluid. Struct. **61**, 168–183 (2016a)

Bell, J.R., Burton, D., Thompson, M.C., Herbst, A.H., Sheridan, J.: Dynamics of trailing vortices in the wake of a generic high-speed train. J. Fluid. Struct. **65**, 238–256 (2016b)

CEN European Standard: Railway Applications-Aerodynamics Part4: Requirements and Test Procedures for Aerodynamics on Open Track. CENEN, pp. 14067–14074 (2013)

Chen, G., Li, X.B., Liu, Z., et al.: Dynamic analysis of the effect of nose length on train aerodynamic performance. J. Wind Eng. Ind. Aerodyn. **184**, 198–208 (2019)

Dong, T., Liang, X., Krajnović, S., Xiong, X., Zhou, W.: Effects of simplifying train bogies on surrounding flow and aerodynamic forces. J. Wind Eng. Ind. Aerodyn. **191**, 170–182 (2019)

Dong, T., Minelli, G., Wang, J., Liang, X., Krajnović, S.: The effect of ground clearance on the aerodynamics of a generic high-speed train. J. Fluids Struct. **95**, 102990 (2020)

Fago, B., Lindner, H., Mahrenholtz, O.: The effect of ground simulation on the flow around vehicles in wind tunnel testing. J. Wind Eng. Ind. Aerodyn. **38**(1), 47–57 (1991)

Flynn, D., Hemida, H., Soper, D., Baker, C.: Detached-eddy simulation of the slipstream of an operational freight train. J. Wind Eng. Ind. Aerodyn. **132**, 1–12 (2014)

Ghasemian, M., Nejat, A.: Aerodynamic noise prediction of a horizontal axis wind turbine using improved delayed detached eddy simulation and acoustic analogy. Energy Convers. Manage. **99**, 210–220 (2015)

Gilbert, T., Baker, C.J., Quinn, A.: Aerodynamic pressures around high-speed trains: the transition from unconfined to enclosed spaces. Proc. Inst. Mech. Eng. Part F. J. Rail Rapid Transp. **227**(6), 609–622 (2013)

Guo, Z.J., Liu, T.H., Chen, Z.W., Xie, T.Z., Jiang, Z.H.: Comparative numerical analysis of the slipstream caused by single and double unit trains. J. Wind Eng. Ind. Aerodyn. **172**, 395–408 (2018)

Hemida, H., Baker, C., Gao, G.: The calculation of train slipstreams using large-eddy simulation. Proc. Inst. Mech. Eng. Part F. J. Rail Rapid Transp. **228**(1), 25–36 (2014)

Hemida, H., Krajnovic, S.: LES study of the influence of the nose shape and yaw angles on flow structures around trains. J. Wind Eng. Ind. Aerodyn. **98**(1), 34–46 (2010)

Hemida, H., Krajnovic, S., Davidson, L.: Large eddy simulations of the flow around a simplified high speed train under the influence of cross-wind. In: 17th AIAA Computational Dynamics Conference, Toronto, Ontario, Canada (2005)

Li, X.B., Chen, G., Wang, Z., Xiong, X.H., Liang, X.F., Yin, J.: Dynamic analysis of the flow fields around single-and double-unit trains. J. Wind Eng. Ind. Aerodyn. **2019**(188), 136–150 (2019)

Menter, F.R.: Two-equation eddy-viscosity turbulence models for engineering applications. AIAA J. **32**, 1598–1605 (2012)

Minelli, G., Yao, H.D., Andersson, N., Höstmad, P., Forssén, J., Krajnović, S.: An aeroacoustic study of the flow surrounding the front of a simplified ICE3 high-speed train model. Appl. Acoust. **160**, 107125 (2020)

Niu, J.Q., Zhou, D., Liang, X.F.: Numerical simulation of the effects of obstacle deflectors on the aerodynamic performance of stationary high-speed trains at two yaw angles. Proc. Inst. Mech. Eng. Part F. J. Rail Rapid Transp. **232**(3), 913–927 (2017)

Popc, C.: Safety of Slipstreams Effects Produced by Trains. A Report Prepared by Mott Macdonald Ltd for Railway Safety and Standards Board, 2nd edn. Mott MacDonald, Croydon (2006)

Shur, M.L., Spalart, P.R., Strelets, M.K., Travin, A.K.: A hybrid RANS-LES approach with delayed-DES and wall-modelled LES capabilities. Int. J. Heat Fluid Flow **29**(6), 1638–1649 (2008)

Spalart, P.R.: Detached-eddy simulation. Ann Rev Fluid Mech. **41**, 181–202 (2009)

Sterling, M., Baker, C.J., Jordan, S.C., Johnson, T.: A study of the slipstreams of high-speed passenger trains and freight trains. Proc. Inst. Mech. Eng. Part F. J. Rail Rapid Transp. **222**(2), 177–193 (2008)

TSI HSRST: Technical specification for interoperability relating to the 'rolling stock'sub-system of the trans-European high-speed rail system. Eur. Law 232 (2008)

Wang, J., Gao, G., Li, X., Liang, X., Zhang, J.: Effect of bogie fairings on the flow behaviours and aerodynamic performance of a high-speed train. Veh. Syst. Dyn. 1–21 (2019a)

Wang, J., Minelli, G., Dong, T., Chen, G., Krajnović, S.: The effect of bogie fairings on the slipstream and wake flow of a high-speed train. An IDDES study. J. Wind Eng. Ind. Aerodyn. **191**, 183–202 (2019)

Wang, J., Minelli, G., Zhang, Y., Zhang, J., Krajnović, S., Gao, G.: An improved delayed detached eddy simulation study of the bogie cavity length effects on the aerodynamic performance of a high-speed train. Proc. Inst. Mech. Eng. Part C: J. Mech. Eng. Sc. 0954406220907631 (2020)

Wang, S.B., Burton, D., Herbst, A.H., John, S., Thompson, M.C.: The effect of the ground condition on high-speed train slipstream. J. Wind Eng. Ind. Aerodyn. **172**, 230–243 (2018a)

Wang, S.B., Burton, D., Herbst, A., John, S.: The effect of bogies on high-speed train slipstream and wake. J. Fluid. Struct. **83**, 471–489 (2018b)

Weise, M.A.R.C.O., Orellano, A., Schober, M.: Slipstream velocities induced by trains. WSEAS Trans. Fluid Mech. **1**(6), 759 (2006)

Wikimedia, C.: N700 series shinkansen prototype set Z0 at Hamamatsu Station on a test run. Online. Available from: https://zh.wikipedia.org/wiki/%E6%96%B0%E5%B9%B9%E7%B7%9A#/media/File:N700_Z0_7881A_Hamamatsu_20060128.jpg (2006)

Xia, C., Shan, X.Z., Yang, Z.G.: Comparison of different ground simulation systems on the flow around a high-speed train. Proc. Inst. Mech. Eng. Part F. J. Rail Rapid Transp. **231**(2), 135–147 (2017a)

Xia, C., Wang, H.F., Shan, X.Z., Yang, Z.G., Li, Q.L.: Effects of ground configurations on the slipstream and near wake of a high-speed train. J. Wind Eng. Ind. Aerodyn. **168**, 177–189 (2017b)

Xie, T.Z., Liu, T.H., Chen, Z.W., Chen, X.D., Li, W.H.: Numerical study on the slipstream and trackside pressure induced by trains with different longitudinal section lines. Proc. Inst. Mech. Eng. Part F. J. Rail Rapid Transp. **232**(6), 1671–1685 (2018)

Yang, G.W., Wei, Y.J., Zhao, G.L., et al.: Current research progress in the mechanics of high speed rails. Adv. Mech. **45**, 201507 (2015)

Zhang, J., Li, J.J., Tian, H.Q., et al.: Impact of ground and wheel boundary conditions on numerical simulation of the high-speed train aerodynamic performance. J. Fluid. Struct. **61**, 249–261 (2016)

Zhang, J., He, K., Xiong, X., Wang, J., Gao, G.: Numerical simulation with a DES approach for a high-speed train subjected to the crosswind. J. Appl. Fluid Mech. **10**(5) (2017)

Zhang, J., Wang, J.B., Wang, Q.X., et al.: A study of the influence of bogie cut outs' angles on the aerodynamic performance of a high-speed train. J. Wind Eng. Ind. Aerodyn. **175**, 153–168 (2018a)

Zhang, L., Yang, M.Z., Liang, X.F.: Experimental study on the effect of wind angles on pressure distribution of train streamlined zone and train aerodynamic forces. J. Wind Eng. Ind. Aerodyn. **174**, 330–343 (2018b)